

# Inverse kinetic isotope effects in the oxygen reduction reaction at platinum single crystals

Received: 31 March 2022

Accepted: 3 October 2022

Published online: 10 November 2022

 Check for updates

Yao Yang<sup>1,4</sup>, Rishi G. Agarwal<sup>2,4</sup>, Phillips Hutchison<sup>2,4</sup>, Rubén Rizo<sup>3,4</sup>, Alexander V. Soudackov<sup>2</sup>, Xinyao Lu<sup>1</sup>, Enrique Herrero<sup>3</sup>✉, Juan M. Felio<sup>3</sup>✉, Sharon Hammes-Schiffer<sup>2</sup>✉, James M. Mayer<sup>2</sup>✉ & Héctor D. Abruña<sup>1</sup>✉

Although the oxygen reduction reaction (ORR) involves multiple proton-coupled electron transfer processes, early studies reported the absence of kinetic isotope effects (KIEs) on polycrystalline platinum, probably due to the use of unpurified D<sub>2</sub>O. Here we developed a methodology to prepare ultra-pure D<sub>2</sub>O, which is indispensable for reliably investigating extremely surface-sensitive platinum single crystals. We find that Pt(111) exhibits much higher ORR activity in D<sub>2</sub>O than in H<sub>2</sub>O, with potential-dependent inverse KIEs of  $\sim 0.5$ , whereas Pt(100) and Pt(110) exhibit potential-independent inverse KIEs of  $\sim 0.8$ . Such inverse KIEs are closely correlated to the lower  $\ast\text{OD}$  coverage and weakened  $\ast\text{OD}$  binding strength relative to  $\ast\text{OH}$ , which, based on theoretical calculations, are attributed to the differences in their zero-point energies. This study suggests that the competing adsorption between  $\ast\text{OH}/\ast\text{OD}$  and  $\ast\text{O}_2$  probably plays an important role in the ORR rate-determining steps that involve a chemical step preceding an electrochemical step (CE mechanism).

One of the key energy conversion systems in nature is photosynthesis, which involves multi-electron, multi-proton transfer processes. Similar to biological reactions, multiple proton-coupled electron transfer (PCET) reactions are critical to many electrochemical reactions for renewable energy technologies such as solar cells, fuel cells, water electrolyzers, and CO<sub>2</sub> and N<sub>2</sub> electroreduction<sup>1,2</sup>. As the most ubiquitous oxidant in nature, oxygen is central to energy systems from biological respiration to fuel cells and combustion. Renewable energy technologies have been unable to match the efficiency of enzymatic systems, in part because key processes—such as the oxygen reduction reaction (ORR) in hydrogen fuel cells—are not yet understood at the atomic level despite decades of investigation. A key tool to probe such electrochemical mechanisms (among others) is the measurement of kinetic isotope effects (KIEs). The most broadly applicable version—for aqueous electrocatalytic processes—involves manipulating reaction

kinetics by substituting protons in the electrolyte with deuterons. This is actually a measurement of the kinetic solvent isotope effect (KSIE) because the solvent is labelled, but for simplicity we will refer to it as the KIE. The H/D KIE value of a reaction is defined as the ratio of the kinetic current in H<sub>2</sub>O to that in D<sub>2</sub>O. Often the KIE for proton transfer and PCET reactions is greater than 1, denoting a normal KIE. An inverse KIE ( $<1$ ) occurs when the activity in D<sub>2</sub>O is higher than that in H<sub>2</sub>O<sup>3</sup>.

Although KIE studies have been attempted in key electrochemical reactions such as hydrogen oxidation/evolution reactions (HOR/HER) and oxygen reduction/evolution reactions (ORR/OER), they remain poorly understood, primarily due to the lack of access to chemically ultra-high-purity D<sub>2</sub>O and well-defined clean single-crystal electrode surfaces—both of which are critical. Addressing these challenges may provide valuable mechanistic insights, for instance, into the extensively studied ORR, which is at the heart of hydrogen fuel cells<sup>4</sup>. The design

<sup>1</sup>Department of Chemistry and Chemical Biology, Cornell University, Ithaca, NY, USA. <sup>2</sup>Department of Chemistry, Yale University, New Haven, CT, USA.

<sup>3</sup>Instituto de Electroquímica, Universidad de Alicante, Alicante, Spain. <sup>4</sup>These authors contributed equally: Yao Yang, Rishi G. Agarwal, Phillips Hutchison, Rubén Rizo. ✉e-mail: [herrero@ua.es](mailto:herrero@ua.es); [juan.felio@ua.es](mailto:juan.felio@ua.es); [sharon.hammes-schiffer@yale.edu](mailto:sharon.hammes-schiffer@yale.edu); [james.mayer@yale.edu](mailto:james.mayer@yale.edu); [hda1@cornell.edu](mailto:hda1@cornell.edu)

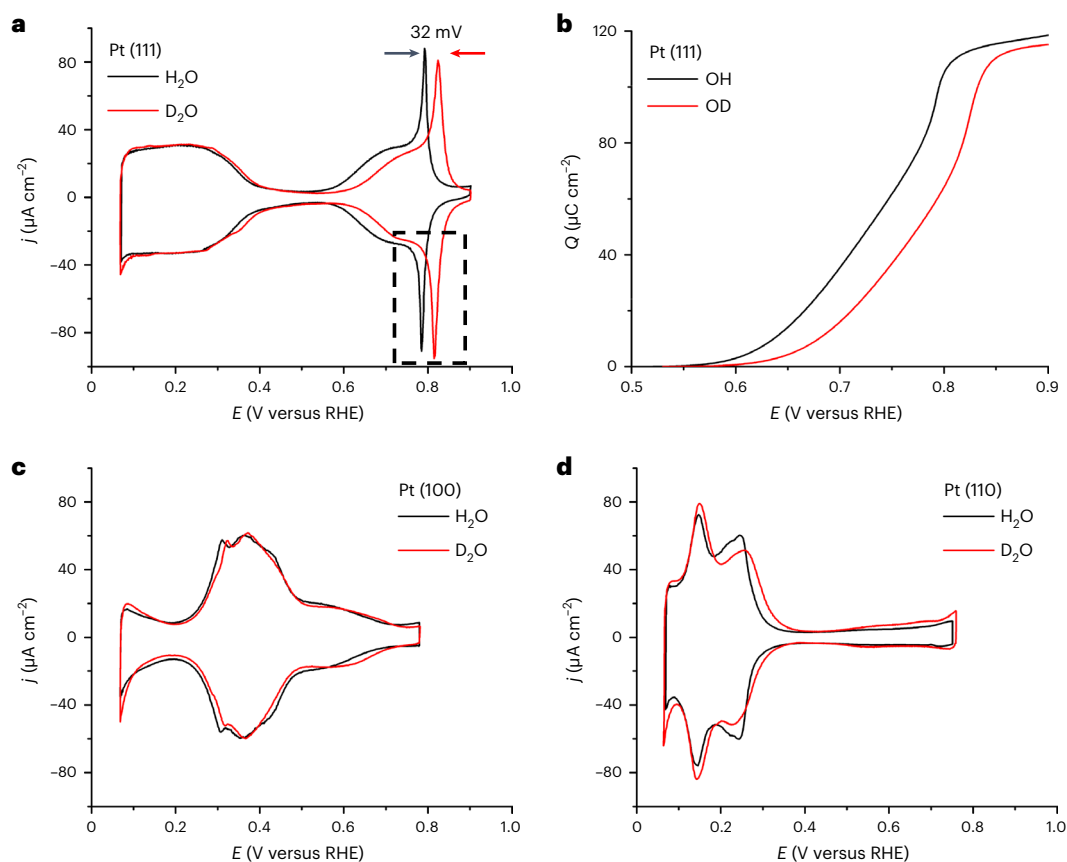


**Fig. 1 | Cyclic voltammetric profiles of platinum single crystals in acidic ultra-high-purity H<sub>2</sub>O and D<sub>2</sub>O.** **a**, Cyclic voltammetric profiles of Pt(111) in argon-saturated 0.1 M HClO<sub>4</sub> in H<sub>2</sub>O and D<sub>2</sub>O showing the OD adsorption/desorption peaks at potentials that were 32 mV more positive than the OH peaks. The sharp

peak (dashed box) observed in the \*OH/\*OD region corresponds to a rapid decay in the coverage. **b**, OH and OD coverage on Pt(111) extracted from the adsorption profiles in **a**. **c,d**, Cyclic voltammetric profiles of Pt(100) (**c**) and stepped Pt(110) (**d**) in argon-saturated 0.1 M HClO<sub>4</sub> in H<sub>2</sub>O and D<sub>2</sub>O.

and development of effective electrocatalysts to accelerate the sluggish ORR have been the main driving force over the past decades to enable fuel cell technologies at scale. After decades of mechanistic studies, it is widely recognized that the rate-determining steps (RDSs) of the ORR involve PCET processes in the formation of key reaction intermediates (HO<sub>2</sub>, H<sub>2</sub>O<sub>2</sub>, OH and so on)<sup>5</sup>; KIE studies are therefore uniquely positioned to provide valuable insights into the PCETs in complex ORR mechanisms.

Pioneering studies since the late 1930s used a variety of polycrystalline metal electrodes to study the KIEs on the HER with purified electrolytes<sup>6–8</sup>. In the 1980s, Yeager et al.<sup>9</sup> performed the first KIE study on the ORR and reported the absence of KIEs for polycrystalline platinum (poly-Pt) in phosphoric acid, which is known to poison platinum surfaces. The majority of later KIE studies on the ORR used commercial D<sub>2</sub>O without further purification and reported no appreciable KIEs, with values of  $1 \pm 0.3$  on poly-Pt, palladium or Pt/C in non-adsorbing acids and bases<sup>4,10,11</sup>. Other ORR studies—again using unpurified D<sub>2</sub>O—reported primary KIEs of 2 or above on Au(100)<sup>12</sup>, metal-containing nitrogen-doped carbon<sup>11,13</sup> and metal oxide nanoparticles<sup>14</sup>. Gewirth et al.<sup>15</sup> reported inverse KIEs of  $-0.5$  on metal oxyhydroxides for the OER in base using unpurified D<sub>2</sub>O and ascribed it to steric effects hindering the further addition of OH on the crowded oxide surface. However, it remains intriguing that noticeable KIEs for the ORR on platinum were absent in those studies, despite the fact that PCET processes are known to play key roles in the ORR kinetics<sup>5</sup>. As the importance of removing organic impurities from H<sub>2</sub>O was realized early<sup>16,17</sup>, ultra-high-purity H<sub>2</sub>O has now been readily accessible after decades of development of water-purification systems;

however, it remains unclear to what extent those KIEs previously reported are complicated by the defects of polycrystalline electrodes and, more importantly, the unknown contamination from commercial, unpurified D<sub>2</sub>O and/or carbon supports for nanoparticle catalysts. Only recently have a few studies attempted to use commercial water-purification systems to purify D<sub>2</sub>O to investigate the ORR on poly-Pt; however, this method remains cost-prohibitive and has not been widely adopted by the community<sup>18</sup>.

In this study we developed a new methodology to prepare chemically ultra-high-purity D<sub>2</sub>O suitable for investigating high-quality platinum single crystals. The use of single-crystal platinum surfaces greatly simplifies the complexity of structure–activity relationships/correlations, and has profoundly shaped and enhanced our fundamental understanding of the ORR mechanism<sup>19</sup>. Here we report inverse KIEs on the ORR in both acid and base at platinum single crystals. This discovery was independently verified by the Cornell and Alicante groups following the same measurement protocols. The inverse KIEs correlate with the much lower coverage of \*OD relative to \*OH at the same applied potentials (the asterisks represent adsorbed species on platinum surfaces). Carbon monoxide stripping measurements provide direct experimental evidence for the lower \*OD coverage and weakened \*OD binding strength relative to \*OH, and the origin of these differences is revealed by periodic density functional theory (DFT) calculations. The inverse KIEs reported here echo the early hypothesis—proposed by Markovic and colleagues 25 years ago<sup>20</sup>—on the inhibiting effects of \*OH to rationalize the ORR activity trends of low-index platinum surfaces. The enhanced ORR kinetics in D<sub>2</sub>O, owing to the lowered \*OD coverage, supports the competing adsorption mechanism of \*OH/\*OD and

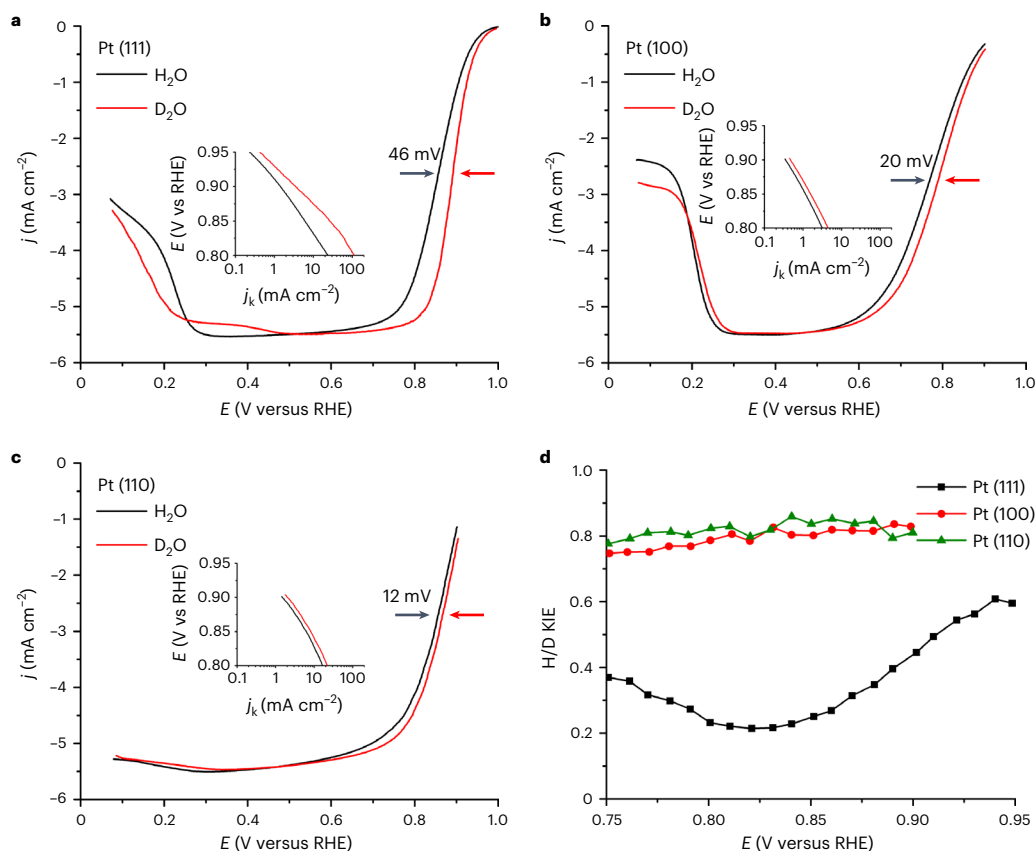


**Fig. 2 | Oxygen reduction reaction kinetics on platinum single crystals in acidic ultra-high-purity H<sub>2</sub>O and D<sub>2</sub>O.** **a**, Oxygen reduction reaction polarization profile for Pt(111). **b**, Oxygen reduction reaction polarization profile for Pt(100). **c**, Oxygen reduction reaction polarization profile for Pt(110). All profiles in O<sub>2</sub>-saturated 0.1 M HClO<sub>4</sub> in H<sub>2</sub>O and D<sub>2</sub>O at 1,600 r.p.m. The insets

show the corresponding Tafel plots. **d**, Corresponding H/D KIEs in acid based on the measured kinetic current density in the Tafel plots. Oxygen reduction reaction kinetics studies on these platinum single crystals in acid exhibit substantially faster ORR kinetics in D<sub>2</sub>O relative to H<sub>2</sub>O, and thus inverse H/D KIEs.

\*O<sub>2</sub>, and provides valuable insights for establishing structure–activity correlations on ORR kinetics.

## Results and discussion

Here we emphasize the stringent requirements for ultra-high electrolyte purity and cleanness of the electrochemical cells; D<sub>2</sub>O was purified using a double-distillation method and treated in an alkaline permanganate solution to remove traces of organic contamination (see Methods for details); platinum single crystals were prepared following Clavilier and colleagues' method<sup>19</sup>, and measured in a hanging meniscus configuration. The cyclic voltammetric (CV) profile of Pt(111) in argon-saturated 0.1 M HClO<sub>4</sub> in H<sub>2</sub>O (acidic H<sub>2</sub>O) shows the characteristic H and OH adsorption/desorption peaks separated by a double-layer region from 0.4 to 0.6 V versus the reversible hydrogen electrode (RHE) (Fig. 1a); OH adsorption (\*OH) in acidic H<sub>2</sub>O exhibits a broad peak at -0.7 V and a sharp reversible peak at 0.792 V, which are associated with the \*OH formation from bulk water with repulsive H<sub>2</sub>O/OH interactions, and with the isolated solvation water surrounding anions with attractive interactions, respectively<sup>21</sup>. The CV profile of Pt(111) in acidic H<sub>2</sub>O shows a \*OH peak current density of above 80 μA cm<sup>-2</sup> and an integrated charge of -120 μC cm<sup>-2</sup>. These values represent criteria of high-quality electrochemistry of Pt(111) single crystals tested in acidic H<sub>2</sub>O (refs. 4,21).

The CV profile of Pt(111) in our acidic D<sub>2</sub>O shows a nearly identical hydrogen adsorption/desorption region, and the OD adsorption (\*OD) region has the same shape as in H<sub>2</sub>O, indicating a similarly clean Pt(111) surface in D<sub>2</sub>O as in H<sub>2</sub>O. However, the \*OD feature at 0.824 V versus

the RHE is positively shifted by 32 mV relative to \*OH in H<sub>2</sub>O (0.792 V) (Fig. 1a). The sharp \*OD peak near 0.8 V exhibits a full-width at half-maximum (FWHM) of -30 mV, indicating a less attractive interaction among \*OD than that among \*OH with a FWHM of -20 mV, given that the FWHM of a non-interacting Langmuir-type adsorption isotherm is 90.6 mV (ref. 21). At 0.9 V, \*OD shows nearly the same integrated charge as \*OH (115 μC cm<sup>-2</sup> versus 118 μC cm<sup>-2</sup>, respectively), which indicates that \*OD and \*OH achieve nearly the same maximum coverage (Fig. 1b); however, at 0.8 V versus the RHE—below the sharp \*OD feature—\*OD has an integrated charge of 65 μC cm<sup>-2</sup>, which is much lower than that of \*OH (105 μC cm<sup>-2</sup>). This indicates a much lower \*OD coverage (θ<sub>OD</sub>) than \*OH coverage (θ<sub>OH</sub>) on platinum at the same applied potentials of less than 0.9 V, and thus more free platinum sites available for O<sub>2</sub> adsorption in D<sub>2</sub>O relative to H<sub>2</sub>O under ORR-relevant conditions (0.7–0.9 V) (Fig. 1b).

The voltammetric profile of Pt(100) in acidic H<sub>2</sub>O exhibits multiple peaks at -0.3 V (Fig. 1c), among which H and OH adsorption processes overlap<sup>22</sup>. Similar to Pt(111), the CV profile of Pt(100) in acidic D<sub>2</sub>O exhibits a very similar hydrogen region to that in acidic H<sub>2</sub>O. Pt(110) can also be characterized as a stepped surface, Pt[2(111) × (111)], containing two-atom-wide (111) terraces separated by monoatomic (111) steps. In this case, it has the highest step density among all platinum single crystals and thus is extremely sensitive to traces of contamination in the electrolyte<sup>23</sup>. The voltammetric profile of Pt(110) in acidic H<sub>2</sub>O shows the characteristic double hydrogen adsorption peaks at 0.15 and 0.25 V versus the RHE (Fig. 1d), which are consistent with previous reports<sup>23</sup>. The CV profile of Pt(110) in fresh acidic D<sub>2</sub>O shows the

same doublet hydrogen peaks as acidic H<sub>2</sub>O; however, the same batch of acidic D<sub>2</sub>O—slightly contaminated after air exposure—would fail to show the second adsorption peak at 0.25 V (Supplementary Fig. 1), which was also noticed in other studies of Pt(110) using commercial D<sub>2</sub>O (ref. 24). In addition to those low-index platinum surfaces, we investigated two stepped platinum single crystals, Pt(322) and Pt(332), with five-atom-wide (111) terraces separated by monoatomic (100) and (110) steps, respectively (Supplementary Fig. 2). Similar to Pt(111), Pt(322) and Pt(332) exhibit nearly the same hydrogen regions in acidic D<sub>2</sub>O as in acidic H<sub>2</sub>O but with positively shifted OD adsorption/desorption peaks relative to the OH peaks in acidic H<sub>2</sub>O, which suggest lower  $\theta_{OD}$  relative to  $\theta_{OH}$  on stepped platinum surfaces at the same applied potentials.

After this thorough investigation of blank CV profiles, ORR kinetics were studied using rotating disk electrode (RDE) voltammetry. Oxygen reduction reaction polarization profiles of platinum single crystals in oxygen-saturated acidic H<sub>2</sub>O and D<sub>2</sub>O are presented in Fig. 2 after iR correction (Supplementary Fig. 3). In acidic D<sub>2</sub>O, Pt(111) shows considerably enhanced ORR kinetics with a half-wave potential ( $E_{1/2}$ ) of 0.890 V versus the RHE, which is 46 mV more positive than that in acidic H<sub>2</sub>O (0.854 V) (Fig. 2a). The ORR kinetic current density and KIEs were calculated following Supplementary equations (1–3). As shown in Fig. 2d, it is counter-intuitive to observe that Pt(111) in acidic D<sub>2</sub>O exhibits KIEs lower than 1, which represents the first report of inverse KIEs for the ORR. The KIEs of Pt(111) in acid show a value of -0.6 at 0.95 V, which decreases to -0.4 at 0.9 V. It then approaches a minimum value of -0.2 at 0.8 V before finally increasing to 0.4 at 0.75 V. The decay of H/D KIE values from 0.9 to 0.8 V (Fig. 2d) coincides with the same potential range over which the difference between  $\theta_{OD}$  and  $\theta_{OH}$  is increasing (Fig. 1b). As highlighted by the dashed box in Fig. 1a, the sharp peak observed in the \*OH/\*OD region corresponds to a rapid decay in the coverage. The rapid decay of  $\theta_{OD}$  starts at 0.9 V and is nearly complete at 0.8 V, which is then followed by the fast decay of  $\theta_{OH}$  from 0.8 to 0.75 V. The minimal KIE plateau of -0.2 at 0.8 V (Fig. 2d) corresponds to a situation in which the differences in the adlayer structure for H<sub>2</sub>O and D<sub>2</sub>O are most significant. At 0.8 V, for \*OD, the species responsible for the sharp peak have been completely desorbed, whereas this value is the onset for the desorption of the corresponding \*OH species (Fig. 1a).

A Tafel analysis provides some insights into possible correlations between ORR kinetics and \*OD and \*OH coverages. The Tafel plot for Pt(111) in acidic H<sub>2</sub>O shows a transition in the Tafel slope from 63 mV dec<sup>-1</sup> (0.95–0.90 V) to -120 mV dec<sup>-1</sup> as the overpotential increases and approaches the diffusion-limited region (Supplementary Fig. 4). Although the origins responsible for this transition are still under debate, one possible mechanism is a RDS that involves a CE process (a chemical step preceding an electrochemical step; Extended Data Fig. 1); the proposition of which is based on in-depth RDE studies and kinetic modeling by Feliu and co-workers<sup>25,26</sup>. At low overpotentials ( $E > 0.9$  V), the RDS is a proton transfer chemical step that involves the formation of HO<sub>2</sub>\* (H<sub>2</sub>O\* + O<sub>2</sub>\* = HO<sub>2</sub>\* + \*OH)<sup>27</sup> when \*OH is dominant and free platinum sites limit the reaction rate. As the overpotential increases,  $\theta_{OH}$  decreases and more platinum sites are available so that the RDS is no longer the chemical step but rather the following electrochemical step (\*OH + H<sup>+</sup> + e<sup>-</sup> = H<sub>2</sub>O), which can explain the Tafel slope of -120 mV dec<sup>-1</sup>—a characteristic value for a 1e<sup>-</sup> RDS<sup>25</sup>. The complete PCET mechanisms during the ORR can be found in our recent review (Supplementary Fig. 5)<sup>5</sup>. In comparison to acidic H<sub>2</sub>O, the Tafel plot for Pt(111) in acidic D<sub>2</sub>O shows a similar slope of 55 mV dec<sup>-1</sup> and a transition

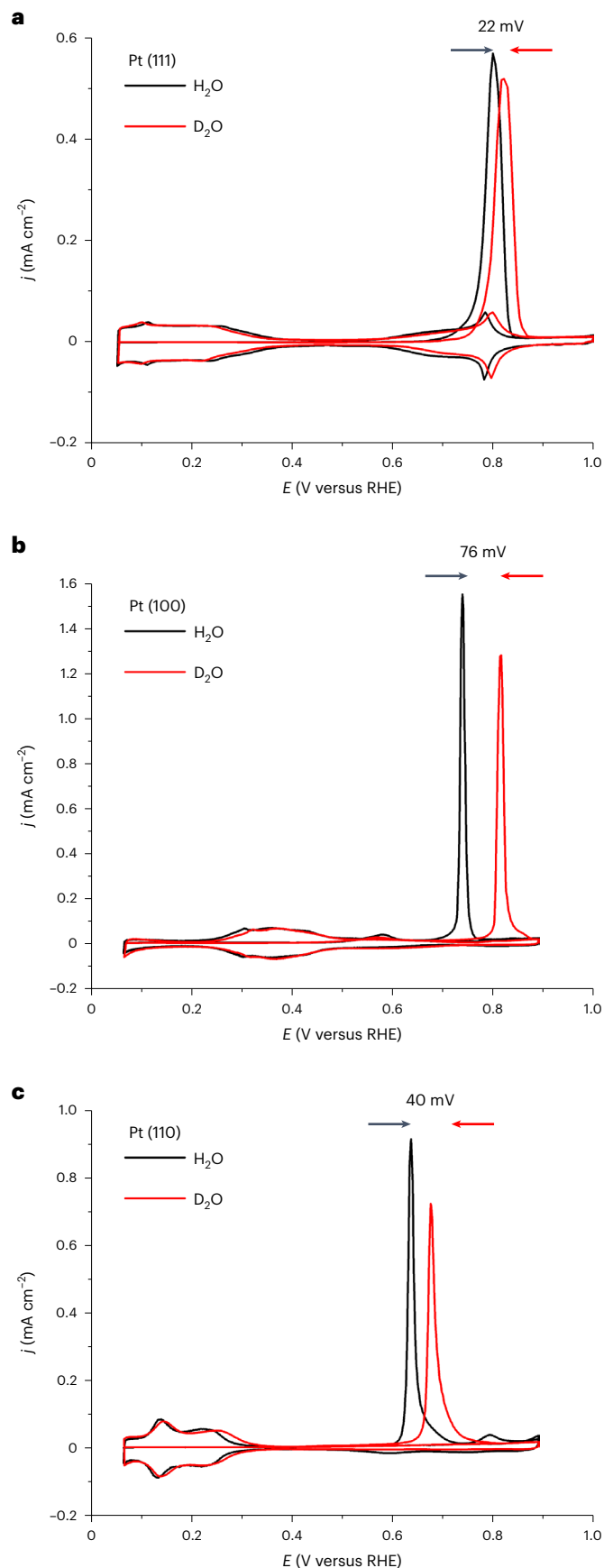


**Fig. 3 | Carbon monoxide electrooxidation kinetics on platinum single crystals in acidic ultra-high-purity H<sub>2</sub>O and D<sub>2</sub>O.** **a**, Carbon monoxide stripping profiles of Pt(111). **b**, CO stripping profiles of Pt(100). **c**, Carbon monoxide stripping profiles of stepped Pt(110). All profiles are in CO-saturated 0.1 M HClO<sub>4</sub> in H<sub>2</sub>O and D<sub>2</sub>O. A more positive CO stripping peak in D<sub>2</sub>O relative to H<sub>2</sub>O provides direct experimental evidence of lower OD coverage and weakened OD binding strength relative to OH at the same applied potentials.

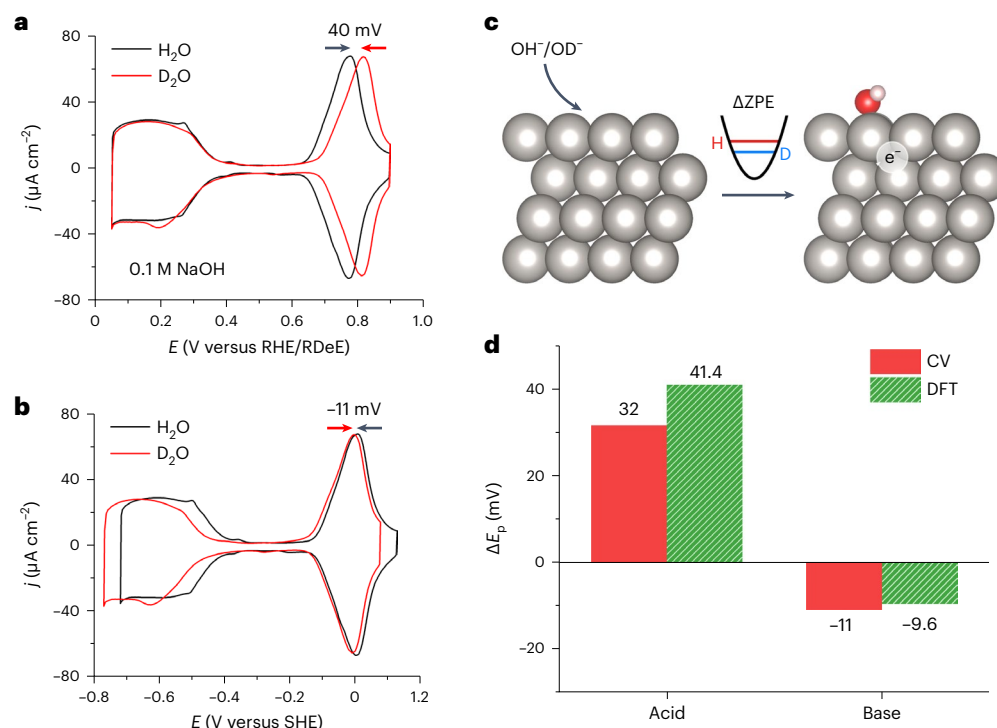


**Fig. 4 | Cyclic voltammetric profiles of Pt(111) in alkaline media and theoretical calculations of OH and OD adsorption.** **a**, Cyclic voltammetric profiles of Pt(111) in argon-saturated 0.1 M NaOH in H<sub>2</sub>O and D<sub>2</sub>O plotted on the RHE/RDeE scale. **b**, Cyclic voltammetric profiles of Pt(111) in argon-saturated 0.1 M NaOH in H<sub>2</sub>O and D<sub>2</sub>O plotted on the SHE scale. The RHE and RDeE are the same in acid but differ by 51 mV in base at pH = 13 (Extended Data Fig. 3). **c**, Schematic of DFT calculations of OH<sup>-</sup> and OD<sup>-</sup> adsorption processes on a

Pt(111) surface with the difference in adsorption free energies mainly due to the differences in the ZPEs of the O–H and O–D stretching modes. **d**, Comparison of experimental (red) and theoretical (green) results of relative OH and OD adsorption peak shifts on Pt(111), based on CV measurements in acid (pH = 1) and base (pH = 13) and corresponding DFT calculations. Note that the adsorption potentials were computed on the SHE (SDE) scale and then converted to the pH (pD)-dependent RHE (RDeE) scale (see Methods for details).

to a similar Tafel slope of  $-120 \text{ mV dec}^{-1}$ , which indicates a similar CE process as the possible RDS in acidic D<sub>2</sub>O. The competing adsorption mechanism between \*O<sub>2</sub> and \*OH/\*OD suggests that \*OH/\*OD coverage is one of the key activity descriptors for rationalizing the enhanced ORR kinetics in acidic D<sub>2</sub>O. We therefore propose that the inverse H/D KIE of Pt(111) is correlated with the lower \*OD coverage compared with \*OH at the same applied potentials under ORR-relevant conditions.

The ORR profiles for Pt(100) in acidic D<sub>2</sub>O show an  $E_{1/2}$  of 0.789 V, which is 20 mV more positive than the  $E_{1/2}$  in acidic H<sub>2</sub>O (0.769 V) (Fig. 2b). Correspondingly, Pt(100) shows an inverse H/D KIE of  $-0.8$  and is largely potential-independent. This is different from the potential-dependent KIE of Pt(111), which may be correlated to the less pronounced differences in the CV profiles of Pt(100) in D<sub>2</sub>O and H<sub>2</sub>O (Fig. 1c). With Pt(110), ORR profiles in acidic D<sub>2</sub>O exhibited an  $E_{1/2}$  of 0.866 V, which is 12 mV more positive relative to acidic H<sub>2</sub>O (0.854 V), and an inverse H/D KIE of  $-0.85$ , similar to that of Pt(100) (Fig. 2c, 2d). Pt(100) and Pt(110) show similar potential-dependent transitions in the Tafel slopes to Pt(111) (Supplementary Table 1). Oxygen reduction reaction kinetics on the most stepped Pt(110) are extremely sensitive to traces of contamination in acidic D<sub>2</sub>O. As shown in Supplementary Fig. 1, after air exposure for a short time, purified D<sub>2</sub>O exhibited greatly deteriorated ORR kinetics and a misleading primary KIE of  $-6$ . In summary, inverse H/D KIEs in acid are observed on all three low-index platinum single crystals, and the potential-dependent KIE on Pt(111) was closely correlated to the interplay of the \*OD and \*OH desorption processes. Overall, the ORR profiles of those three platinum single crystals in acidic solutions showed similar ORR activity trends in H<sub>2</sub>O and D<sub>2</sub>O: Pt(111)  $\approx$  Pt(110)  $\gg$  Pt(100), consistent with previous reports in acid (Extended Data Fig. 2 and Supplementary Table 2)<sup>22,28</sup>.

To provide additional insights into \*OD and \*OH interactions on platinum single crystals, CO stripping was employed as a molecular probe because CO electrooxidation needs to be triggered by an adsorbed reactive hydroxyl species<sup>29</sup>. Electrooxidation of a monolayer of CO on Pt(111) in acidic H<sub>2</sub>O exhibits a sharp CO stripping peak centered at 0.799 V versus the RHE (Fig. 3a). In comparison, the CO stripping peak potential of Pt(111) in acidic D<sub>2</sub>O is located at 0.821 V, which is 22 mV more positive than that in acidic H<sub>2</sub>O. This serves as direct evidence that \*OD has a lower binding strength on Pt(111) relative to \*OH, rendering the initial adsorption of OD more difficult, and requiring higher overpotentials to complete the electrooxidation of CO in acidic D<sub>2</sub>O (ref. 30). The weakened \*OD binding strength on Pt(111) is consistent with the lower \*OD coverages at the same potentials observed in the voltammetric profile in Fig. 1a. Carbon monoxide stripping on Pt(100) in acidic D<sub>2</sub>O also takes place at the much more positive potential of 0.815 V, which is 76 mV higher than in acidic H<sub>2</sub>O (0.739 V) (Fig. 3b). Similarly, the CO oxidation peak potential on Pt(110) is located at 0.676 V, with a 40 mV positive shift relative to acidic H<sub>2</sub>O (0.636 V) (Fig. 3c). Carbon monoxide stripping measurements of all three low-index platinum surfaces in acidic D<sub>2</sub>O show nearly the same FWHM and CO integrated charge as in acidic H<sub>2</sub>O (Supplementary Tables 3–5), suggesting similarly attractive interactions and maximum CO coverages<sup>30</sup>. The CO stripping results on Pt(100) and Pt(110) provide valuable complementary indications of the weakened \*OD binding strength, which were not readily evident in the CV measurements on those two platinum surfaces (Fig. 1c,d). In summary, CV and CO stripping measurements provide direct experimental evidence that the lower \*OD coverage and weakened \*OD binding strength are the key activity descriptors for rationalizing the inverse KIEs for the ORR in acid.

Although the ORR mechanism is not as well understood in alkaline media as it is in acid, a similar ORR reaction pathway has been proposed (Supplementary Fig. 5). Given the formidable challenges of maintaining ultra-high-purity alkaline D<sub>2</sub>O, particularly for stepped Pt(110), we only present what we consider to be reliable electrochemical studies of Pt(111) in alkaline media. As shown in Fig. 4a, the voltammetric profile of Pt(111) in 0.1 M NaOH/H<sub>2</sub>O (alkaline H<sub>2</sub>O) shows a reversible \*OH adsorption peak centred at 0.777 V versus the RHE, which is consistent with early reports<sup>31</sup>. The CV profile of Pt(111) in alkaline D<sub>2</sub>O shows a much more positive \*OD peak potential at 0.817 V versus the reversible deuterium electrode (RDeE). This is a 40 mV positive shift relative to alkaline H<sub>2</sub>O, which is similar to the positive shift of Pt(111) in acid (Fig. 1a). Furthermore, the CV profile in alkaline D<sub>2</sub>O exhibits a FWHM of 110 mV, which is nearly identical to that in alkaline H<sub>2</sub>O (109 mV), indicating that both \*OD and \*OH on Pt(111) in alkaline media experience small repulsive interactions. Although the potential values of RHE and RDeE are the same in acid, they differ by 51 mV at pH = 13 given that the pK<sub>a</sub> of H<sub>2</sub>O is 14 at 25 °C whereas the pK<sub>a</sub> of D<sub>2</sub>O is 14.87, and thus the pH of 0.1 M NaOH/H<sub>2</sub>O is 13 whereas the pD of 0.1 M NaOH/D<sub>2</sub>O is 13.87 (Extended Data Fig. 3)<sup>18</sup>. After replotting the CV profiles on the absolute standard hydrogen electrode (SHE) scale, the CV profile of Pt(111) in alkaline D<sub>2</sub>O shows that the \*OD peak is shifted by -11 mV relative to alkaline H<sub>2</sub>O (Fig. 4b). The standard deuterium electrode (SDE) is assumed to be equivalent to the SHE in the analysis of both the experimental and computational data (see equations (10) and (11) in the Methods). Oxygen reduction reaction profiles for Pt(111) in alkaline D<sub>2</sub>O indicate an E<sub>1/2</sub> of 0.928 V versus the RDeE, which is 47 mV more positive than in alkaline H<sub>2</sub>O (0.881 V versus the RHE) (Supplementary Fig. 6). The KIEs of Pt(111) in alkaline media show an inverse KIE value of -0.4 on the RHE/RDeE scale, which is close to the inverse KIE value of Pt(111) in acidic media (Extended Data Fig. 4a). The inverse KIEs of Pt(111) in alkaline media can also be rationalized by the substantially lower \*OD coverage relative to \*OH in alkaline media at the same applied potentials under ORR-relevant conditions (Extended Data Fig. 4b).

Theoretical calculations offer possible explanations for the positive shift of the \*OD peaks relative to the \*OH peaks in both acid and base. As discussed already, this shift is interpreted to be responsible for the inverse KIEs for the ORR on platinum single crystals. Periodic DFT calculations were used to calculate the relative equilibrium potentials for adsorbing OH<sup>-</sup> or OD<sup>-</sup> on the Pt(111) surface to produce \*OH or \*OD, respectively (Fig. 4c)<sup>32,33,34</sup>. These relative equilibrium potentials were determined according to equation (9) (see Methods; computational details can be found in the Supplementary Information). The major contribution to this relative equilibrium potential is the difference in the zero-point energies (ZPEs) associated with the O–H and O–D stretching modes of the molecular and adsorbed species. These calculations predict that the \*OD peak would be shifted by -9.6 mV relative to the \*OH peak (Fig. 4d) after taking into account the offset of  $eE_{\text{RDeE}} - eE_{\text{RHE}}$  (Extended Data Fig. 3). This shift is consistent with the -11 mV shift observed in the CV profiles of Pt(111) measured in 0.1 M NaOH (Fig. 4b). These calculations also predict that the \*OD peak would be shifted by 41.4 mV relative to the \*OH peak in acid (Fig. 4d), which is in reasonable agreement with the experimentally measured peak shift of 32 mV in the CV profiles in 0.1 M HClO<sub>4</sub> (Fig. 1a). Similar results were obtained for two different functionals and two different surface coverages (Supplementary Table 11). Density functional theory calculations therefore suggest that the experimentally observed weakened \*OD binding strength, relative to \*OH correlates to the difference in the ZPEs of the adsorbed and molecular species.

In conclusion we present the observation of substantially higher ORR activity in D<sub>2</sub>O relative to H<sub>2</sub>O, corresponding to inverse H/D KIEs at well-defined platinum single-crystal surfaces. These results were enabled by the use of ultra-high-purity D<sub>2</sub>O and well-defined single-crystal platinum surfaces. Potential-dependent KIEs of Pt(111)

were closely correlated to the interplay of \*OD and \*OH desorption processes with much lower \*OD coverage and weakened \*OD binding strength relative to \*OH at the same applied potentials. We propose an activity–structure correlation in which inverse KIEs arise from fundamental differences in the ZPEs with the main contributions arising from the O–D and O–H stretching modes. Further operando/ in situ experimental and computational efforts could advance our understanding of the interplay between OD/OH and interfacial water structure, and their impact on ORR kinetics (see the Supplementary Notes for a discussion on the possible role of hydrogen bonding); \*OH and \*OD are expected to play an important role in the KIE effects of HOR/HER kinetics, as suggested by the presence of \*OH adsorption in the hydrogen regions of platinum<sup>35–38</sup>. The strategy of studying platinum single crystals in ultra-high-purity D<sub>2</sub>O electrolyte provides previously inaccessible insights into the kinetics of ORR, specifically the origin of the unusual inverse KIE, and is broadly applicable to a wide range of other electrochemical reactions involving multiple PCET processes.

## Online content

Any methods, additional references, Nature Research reporting summaries, source data, extended data, supplementary information, acknowledgements, peer review information; details of author contributions and competing interests; and statements of data and code availability are available at <https://doi.org/10.1038/s41557-022-01084-y>.

## References

1. Warburton, R. E., Soudackov, A. V. & Hammes-Schiffer, S. Theoretical modeling of electrochemical proton-coupled electron transfer. *Chem. Rev.* **122**, 10599–10650 (2022).
2. Agarwal, R. G. et al. Free energies of proton-coupled electron transfer reagents and their applications. *Chem. Rev.* **122**, 1–49 (2022).
3. George, T. Y., Asset, T., Avid, A., Atanassov, P. & Zenyuk, I. V. Kinetic isotope effect as a tool to investigate the oxygen reduction reaction on Pt-based electrocatalysts—part I: high-loading Pt/C and Pt extended surface. *ChemPhysChem* **21**, 469–475 (2020).
4. Gómez-Marín, A. M., Rizo, R. & Feliu, J. M. Oxygen reduction reaction at Pt single crystals: a critical review. *Catal. Sci. Technol.* **4**, 1685–1698 (2014).
5. Yang, Y. et al. Electrocatalysis in alkaline media and alkaline membrane-based energy technologies. *Chem. Rev.* **122**, 6117–6321 (2022).
6. Bawn, C. E. H. & Ogden, G. Wave mechanical effects and the reactivity of the hydrogen isotopes. *Trans. Faraday Soc.* **30**, 432–443 (1934).
7. Conway, B. E. & Steacie, E. W. R. Kinetics of electrolytic hydrogen and deuterium evolution. *Proc. R. Soc. A.* **256**, 128–144 (1960).
8. Bockris, J. O. M. & Matthews, D. B. Proton tunneling in the hydrogen evolution reaction. *J. Chem. Phys.* **44**, 298–309 (1966).
9. Ghoneim, M. M., Clouser, S. & Yeager, E. Oxygen reduction kinetics in deuterated phosphoric acid. *J. Electrochem. Soc.* **132**, 1160–1162 (1985).
10. Tse, E. C. M., Varnell, J. A., Hoang, T. T. H. & Gewirth, A. A. Elucidating proton involvement in the rate-determining step for Pt/Pd-based and non-precious-metal oxygen reduction reaction catalysts using the kinetic isotope effect. *J. Phys. Chem. Lett.* **7**, 3542–3547 (2016).
11. Chen, Y., Asset, T., Lee, R., Artyushkova, K. & Atanassov, P. Kinetic isotopic effect studies of iron–nitrogen–carbon electrocatalysts for oxygen reduction reaction. *J. Phys. Chem. C* **123**, 11476–11483 (2019).
12. Mei, D. et al. Mechanistic and kinetic implications on the ORR on a Au(100) electrode: pH, temperature and H–D kinetic isotope effects. *Phys. Chem. Chem. Phys.* **16**, 13762–13773 (2014).

13. Malko, D. & Kucernak, A. Kinetic isotope effect in the oxygen reduction reaction (ORR) over Fe–N/C catalysts under acidic and alkaline conditions. *Electrochem. Commun.* **83**, 67–71 (2017).
14. Wang, Y. et al. Synergistic Mn–Co catalyst outperforms Pt on high-rate oxygen reduction reaction for alkaline polymer electrolyte fuel cells. *Nat. Commun.* **10**, 1506 (2019).
15. Tse, E. C. M., Varnell, J. A., Hoang, T. T. H. & Gewirth, A. A. Observation of an inverse kinetic isotope effect in oxygen evolution electrochemistry. *ACS Catal.* **6**, 5706–5714 (2016).
16. Conway, B. E., Angerstein-Kozłowska, H., Sharp, W. B. A. & Criddle, E. E. Ultrapurification of water for electrochemical and surface chemical work by catalytic pyrodistillation. *Anal. Chem.* **45**, 1331–1336 (1973).
17. Hetland, E. Electrolytic conductivity of NaOH in H<sub>2</sub>O and of NaOD in D<sub>2</sub>O at 25°. A vacuum distilling apparatus for deuterium oxide. *J. Am. Chem. Soc.* **68**, 2532–2535 (1946).
18. Sakaushi, K. Quantum proton tunneling in multielectron/-proton transfer electrode processes. *Faraday Discuss.* **221**, 428–448 (2020).
19. Orts, J. M., Gomez, R., Feliu, J. M., Aldaz, A. & Clavilier, J. Potentiostatic charge displacement by exchanging adsorbed species on Pt(111) electrodes-acidic electrolytes with specific anion adsorption. *Electrochim. Acta* **39**, 1519–1524 (1994).
20. Markvoic, N. M., Gasteiger, H. A. & Ross, P. N. Kinetics of oxygen reduction on Pt(hkl) electrodes: implications for the crystallite size effect with supported Pt electrocatalysts. *J. Electrochem. Soc.* **144**, 1591–1597 (1997).
21. Berna, A., Climent, V. & Feliu, J. M. New understanding of the nature of OH adsorption on Pt(111) electrodes. *Electrochem. Commun.* **9**, 2789–2794 (2007).
22. Arán-Ais, R. M. et al. On the behavior of the Pt(100) and vicinal surfaces in alkaline media. *Electrochim. Acta* **58**, 184–192 (2011).
23. Attard, G., Souza-Garcia, J., Martínez-Hincapié, R. & Feliu, J. M. Nitrate anion reduction in aqueous perchloric acid as an electrochemical probe of Pt{110}-(1×1) terrace sites. *J. Catal.* **378**, 238–247 (2019).
24. Rebollar, L., Intikhab, S., Snyder, J. D. & Tang, M. H. Kinetic isotope effects quantify pH-sensitive water dynamics at the Pt electrode interface. *J. Phys. Chem. Lett.* **11**, 2308–2313 (2020).
25. Gómez-Marín, A. M., Feliu, J. M. & Ticianelli, E. Oxygen reduction on platinum surfaces in acid media: experimental evidence of a CECE/DISP initial reaction path. *ACS Catal.* **9**, 2238–2251 (2019).
26. Gómez-Marín, A. M., Feliu, J. M. & Ticianelli, E. Reaction mechanism for oxygen reduction on platinum: existence of a fast initial chemical step and a soluble species different from H<sub>2</sub>O<sub>2</sub>. *ACS Catal.* **8**, 7931–7943 (2018).
27. Dong, J. et al. In situ Raman spectroscopic evidence for oxygen reduction reaction intermediates at platinum single-crystal surfaces. *Nat. Energy* **4**, 60–67 (2019).
28. Briega-Martos, V., Herrero, E. & Feliu, J. M. Effect of pH and water structure on the oxygen reduction reaction on platinum electrodes. *Electrochim. Acta* **241**, 497–509 (2017).
29. Zhuang, L., Jin, J. & Abruña, H. D. Direct observation of electrocatalytic synergy. *J. Am. Chem. Soc.* **129**, 11033–11035 (2007).
30. Gómez, R., Feliu, J. M., Aldaz, A. & Weaver, M. J. Validity of double-layer charge-corrected voltammetry for assaying carbon monoxide coverages on ordered transition metals: comparisons with adlayer structures in electrochemical and ultrahigh vacuum environments. *Surf. Sci.* **410**, 48–61 (1998).
31. Rizo, R., Herrero, E. & Feliu, J. M. Oxygen reduction reaction on stepped platinum surfaces in alkaline media. *Phys. Chem. Chem. Phys.* **15**, 15416–15425 (2013).
32. McCrum, I. T. & Janik, M. J. pH and Alkali cation effects on the Pt cyclic voltammogram explained using density functional theory. *J. Phys. Chem. C* **120**, 457–471 (2016).
33. Nørskov, J. K. et al. Origin of the overpotential for oxygen reduction at a fuel-cell cathode. *J. Phys. Chem. B* **108**, 17886–17892 (2004).
34. Hansen, H. A., Rossmeisl, J. & Nørskov, J. K. Surface Pourbaix diagrams and oxygen reduction activity of Pt, Ag and Ni(111) surfaces studied by DFT. *Phys. Chem. Chem. Phys.* **10**, 3722–3730 (2008).
35. McCrum, I. T., Chen, X., Schwarz, K. A., Janik, M. J. & Koper, M. T. M. Effect of step density and orientation on the apparent pH dependence of hydrogen and hydroxide adsorption on stepped platinum surfaces. *J. Phys. Chem. C* **122**, 16756–16764 (2018).
36. van der Niet, M. J. T. C., Garcia-Araeza, N., Hernández, J., Feliu, J. M. & Koper, M. T. M. Water dissociation on well-defined platinum surfaces: the electrochemical perspective. *Catal. Today* **202**, 105–113 (2013).
37. Rizo, R. et al. Investigating the presence of adsorbed species on Pt steps at low potentials. *Nat. Commun.* **13**, 2550 (2022).
38. Garcia-Araeza, N., Climent, V. & Feliu, J. M. Analysis of temperature effects on hydrogen and OH adsorption on Pt(111), Pt(100) and Pt(110) by means of Gibbs thermodynamics. *J. Electroanal. Chem.* **649**, 69–82 (2010).

**Publisher's note** Springer Nature remains neutral with regard to jurisdictional claims in published maps and institutional affiliations.

Springer Nature or its licensor (e.g. a society or other partner) holds exclusive rights to this article under a publishing agreement with the author(s) or other rightsholder(s); author self-archiving of the accepted manuscript version of this article is solely governed by the terms of such publishing agreement and applicable law.

© The Author(s), under exclusive licence to Springer Nature Limited 2022

## Methods

### Materials

Ultra-pure water (Milli-Q water system); deuterium water (D<sub>2</sub>O, Sigma-Aldrich 99.9 at% Deuterium); HClO<sub>4</sub> (70%, Suprapur); NaOH-H<sub>2</sub>O (99.99% Suprapur); KOH (Sigma-Aldrich, semiconductor grade); KMnO<sub>4</sub> (Sigma-Aldrich, ACS reagent, ≥99%, low in mercury); and platinum wire (Goodfellow, Diameter = 5 mm, 99.995%) were used, as well as argon, O<sub>2</sub> and CO gases (ultra-high-purity, Airgas).

### Purification of deuterium oxide

The purity of chemicals and cleanness of experimental apparatus are critical for the rigorous electrochemical measurements of platinum single crystals. Here we describe a new methodology for the preparation of batch-scale deuterium oxide suitable for voltametric investigations of these surfaces in both acidic and alkaline electrolytes.

Commercial Milli-Q water systems such as the one used in this study are commonly employed to purify H<sub>2</sub>O using an ion-exchange resin and activated carbon columns before applying a ultraviolet light treatment and 0.22 μm filter to remove bacteria. The resulting H<sub>2</sub>O has a resistivity of >18 MΩ cm and <5 ppb total organic carbon<sup>39,40</sup>. Our preparation of deuterium oxide takes inspiration from this methodology, as well as a method for producing conductivity-grade water by distilling it before adding sodium hydroxide and potassium permanganate, and then distilling again<sup>41</sup>. The logic behind this procedure is to remove ions via distillation and to oxidize trace organics to non-volatile species so that they too can be removed via distillation.

Commercial D<sub>2</sub>O was passed through a home-built glass ion-exchange resin column. The glass column contained a low total organic carbon mixed cation and anion-exchange resin (UCW3700, Polysciences), which exchanges ionic impurities for H<sup>+</sup> or OH<sup>-</sup>. To improve product isotopic purity, 200 g of D<sub>2</sub>O was run through the column before use and the column was kept sealed when not in use. After filtering the D<sub>2</sub>O through the ion-exchange resin column, 0.35 wt% KOH and 0.05 wt% KMnO<sub>4</sub> were added. The resulting mixture was distilled using a short-path distillation head with 14/20 joints. Distillations were performed using 2 × 100 g bottles of D<sub>2</sub>O starting material with a 300 ml round-bottom distillation flask and a 250 ml receiving flask under N<sub>2</sub> flow to prevent CO<sub>2</sub> contamination. The yield for this procedure was ~180 g of purified D<sub>2</sub>O, or ~90%. The remaining 20 ml was lost due to N<sub>2</sub> flow or left in the distillation flask to prevent KMnO<sub>4</sub> from coming over in the set-up. In our experience, the flask is too hot and may bump KMnO<sub>4</sub> residue across the distillation head when the KMnO<sub>4</sub> residue in the round-bottom flask turns from deep purple to turquoise. If this colour change is seen, the heat must be lowered or the distillation should be stopped to prevent contamination of the product by KMnO<sub>4</sub>. Final products were stored in flame-sealed 50 ml glass ampoules.

This procedure is successful when several experimental precautions are taken. To avoid contamination or sticking between ground glass joints, all joints that might reasonably come into contact with D<sub>2</sub>O were sealed with PTFE sleeves. All glassware used (and the PTFE sleeves) were cleaned following a previously reported method<sup>42</sup>. Briefly, the glassware were soaked overnight in a solution containing 1 g l<sup>-1</sup> KMnO<sub>4</sub> and 0.5 M H<sub>2</sub>SO<sub>4</sub>, before decanting and dissolving remaining MnO<sub>2</sub> in dilute piranha etch solution. Dilute piranha etch solutions were prepared by adding H<sub>2</sub>SO<sub>4</sub> (Sigma-Aldrich, 95–98%, ACS reagent) and H<sub>2</sub>O<sub>2</sub> (Fisher, 30 wt%, Certified ACS) slowly to water, as opposed to diluting the concentrated mixture which can present a considerable safety hazard. Glassware was then boiled three times in ultra-pure water from a Synergy-R Millipore system and flame-dried before use. The isotopic purity of the D<sub>2</sub>O product was measured to be 95 at% D by mass spectrometry. See ref. <sup>43</sup> for the full details.

### Electrochemical measurements of platinum single crystals

Pt(111), (100), (110), (332) and (322) were fabricated from platinum wires by the Clavilier method<sup>44</sup>. Before each experiment, the electrode was

annealed in a propane flame for 15 s. The hot electrode was then cooled down in a 30% hydrogen balance argon gas atmosphere, quenched in H<sub>2</sub>-saturated ultra-pure water and immediately transferred to the electrochemical cell, which is protected by an ultra-pure water droplet on top of the electrode surface; 30% H<sub>2</sub>/Ar was selected here for all platinum single crystals to ensure the same reducing cooling environments. The effects of the cooling environments—particularly for Pt(110)—can be found in our early reports<sup>45</sup>. The electrochemical cell and all of the other glassware used in the experiment were soaked in KMnO<sub>4</sub>/H<sub>2</sub>SO<sub>4</sub> solution overnight and cleaned right before electrochemical measurements. The remaining KMnO<sub>4</sub>/H<sub>2</sub>SO<sub>4</sub> solution on the glassware was removed by reacting with H<sub>2</sub>O<sub>2</sub> (-1 wt%) before the experiment. The glassware were then rinsed with ultra-pure water, followed by boiling in ultra-pure water three times. Cyclic voltammetric profiles of platinum single crystals were performed at 25 °C using a Pine potentiostat in a three-electrode electrochemical cell with glass frits (mesh 0.5 μm) serving as a salt bridge between the working electrode with the reference electrode to minimize potential chloride contamination. A carbon rod (D = 1.0 cm, L = 5 cm) was used as the counter electrode, and Ag/AgCl in 1 M KCl (0.235 V versus the SHE) was used as the reference electrode. The platinum single-crystal working electrode was in contact with the electrolyte in the hanging meniscus configuration for both CV measurements of stationary electrodes and RDE measurements under a constant rotation rate of 1,600 r.p.m. Carbon monoxide stripping measurements were performed by flowing CO gas at a CO dosing potential of 0.1 V versus the RHE for 5 min followed by an argon purge for 20 min. All electrochemical measurements were reproduced at least three times. The findings in this work were independently verified by the Cornell and Alicante groups following the same measurement protocols.

It should be noted that the amount of proton in HClO<sub>4</sub> added in D<sub>2</sub>O is negligible given that the chemically purified D<sub>2</sub>O has an isotopic purity of 95 at% D and HClO<sub>4</sub> is diluted in D<sub>2</sub>O by a factor of ~500. The use of HClO<sub>4</sub> both in H<sub>2</sub>O and D<sub>2</sub>O ensures the same low levels of impurities given that DClO<sub>4</sub> may introduce more undesirable impurities in deuterated electrolytes.

### DFT calculations of relative equilibrium potentials

We used periodic DFT to calculate the relative equilibrium potentials for adsorbing OH or OD on the Pt(111) surface<sup>32–34,46</sup>. In this process, OL<sup>-</sup> (L = H or D) adsorbs on a bare surface site (\*) to form \*OL and transfers an electron to the external circuit. The reaction of interest is



The adsorption free energy of this reaction is

$$\begin{aligned} \Delta G_{\text{ads}} &= G_{*\text{OL}} + \bar{\mu}_{e^-} - (G_* + G_{\text{OL}^-}) \\ &= G_{*\text{OL}} - eE - (G_* + G_{\text{OL}^-}) \end{aligned} \quad (2)$$

Here  $\bar{\mu}_{e^-} = -eE$  is the electrochemical potential of the electron, where  $e$  is the elementary charge and  $E$  is the electrode potential relative to vacuum. The adsorption equilibrium potential ( $E_{\text{ads}}$ ) can be obtained under equilibrium conditions (where  $\Delta G_{\text{ads}} = 0$ ) from the following expression:

$$eE_{\text{ads}} = G_{*\text{OL}} - (G_* + G_{\text{OL}^-})$$

Our goal is to calculate the relative equilibrium potential ( $\Delta E_{\text{ads}}$ ) for D and H:

$$e\Delta E_{\text{ads}} = (G_{*\text{OD}} - G_{*\text{OH}}) - (G_{\text{OD}^-} - G_{\text{OH}^-}) \quad (4)$$

The free energy of a species can be calculated as the sum of the DFT electronic energy ( $U_{\text{DFT}}$ ) and the ZPE and thermal entropy

(*TS*) contributions:

$$G = U_{\text{DFT}} + \text{ZPE} - TS \quad (5)$$

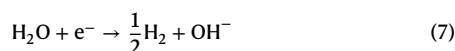
The ZPE and vibrational entropy contributions are obtained from vibrational normal mode analysis. For strongly chemisorbed species, the translational and rotational contributions to the entropy are negligible and therefore are not included in these calculations, although these contributions are included for the solvated molecular species.

As the DFT electronic energies are the same for isotopologues,  $E_{\text{ads}}$  can be expressed in terms of changes in the ZPE and *TS* contributions:

$$e\Delta E_{\text{ads}} = (\Delta \text{ZPE}_{\text{ads}} - T\Delta S_{\text{ads}}) - (\Delta \text{ZPE}_{\text{mol}}(\text{OL}^-) - T\Delta S_{\text{mol}}(\text{OL}^-)) \quad (6)$$

Here the terms are grouped into adsorbed species and solution phase molecular species, where  $\Delta \text{ZPE}_{\text{ads}} = \text{ZPE}_{\text{OD}} - \text{ZPE}_{\text{OH}}$  and  $\Delta \text{ZPE}_{\text{mol}}(\text{OL}^-) = \text{ZPE}_{\text{OD}^-} - \text{ZPE}_{\text{OH}^-}$ . The entropic terms  $T\Delta S_{\text{ads}}$  and  $T\Delta S_{\text{mol}}$  are defined analogously. Here the subscript ‘mol’ refers to solvated molecular species, whereas the  $\text{OL}^-$  in parentheses refers to the specific species  $\text{OD}^-$  and  $\text{OH}^-$ .

To avoid complications associated with applications of periodic DFT to charged systems, the free energy of  $\text{OH}^-$  (or  $\text{OD}^-$ ) can be computed in terms of the free energies of  $\text{H}_2\text{O}$  and  $\text{H}_2$  (or  $\text{D}_2\text{O}$  and  $\text{D}_2$ ). The RHE reaction in alkaline conditions can be written as<sup>32</sup>



At equilibrium, the free energy of  $\text{OH}^-$  on the RHE scale may be expressed as

$$G_{\text{OH}^-} = G_{\text{H}_2\text{O}} - \left(\frac{1}{2}G_{\text{H}_2} + eE_{\text{RHE}}\right) \quad (8)$$

The free energy of  $\text{OD}^-$  on the RDeE scale can be expressed analogously. Here,  $E_{\text{RHE}}$  and  $E_{\text{RDeE}}$  are the equilibrium potentials for the RHE and the RDeE, respectively. Substituting these expressions into equation (6) allows us to write the final equation for the difference in equilibrium potentials for  $\text{OD}^-$  and  $\text{OH}^-$  adsorption as

$$e\Delta E_{\text{ads}} = (\Delta \text{ZPE}_{\text{ads}} - T\Delta S_{\text{ads}}) - \left(\Delta \text{ZPE}_{\text{mol}}(\text{L}_2\text{O}) - T\Delta S_{\text{mol}}(\text{L}_2\text{O}) - \frac{1}{2}\Delta \text{ZPE}_{\text{mol}}(\text{L}_2) + \frac{1}{2}T\Delta S_{\text{mol}}(\text{L}_2)\right) + (eE_{\text{RDeE}} - eE_{\text{RHE}}) \quad (9)$$

The offset between the RHE and RDeE scales can be determined by the following expressions<sup>32–34</sup>:

$$eE_{\text{RHE}} = eE_{\text{SHE}} - k_{\text{B}}T \ln(10) \text{ pH} \quad (10)$$

$$eE_{\text{RDeE}} = eE_{\text{SDE}} - k_{\text{B}}T \ln(10) \text{ pD} \quad (11)$$

Here,  $E_{\text{SHE}}$  and  $E_{\text{SDE}}$  are the equilibrium potentials for the SHE and SDE reactions, which are assumed to be equivalent in the analysis of both the experimental and computational data for consistency, although they differ slightly in the range of 5.8 to 13 mV (refs. 13,47). Including this effect will not alter the qualitative conclusions of this work. For  $\text{pH} = \text{pD} = 1$ , the offset  $eE_{\text{RDeE}} - eE_{\text{RHE}}$  is 0 meV, whereas for  $\text{pH} = 13$  and  $\text{pD} = 13.87$ , this offset is  $-51$  meV (refs. 48,49).

### Computational details

All periodic DFT calculations were performed using the Quantum ESPRESSO package<sup>50,51</sup>. The main calculations used the revPBE functional with dispersion corrections (revPBE-D3)<sup>52,53</sup>. Further calculations were performed with the Perdew–Burke–Ernzerhof (PBE) functional

with dispersion corrections (PBE-D3)<sup>53,54</sup> to test the functional dependency, and the results did not change considerably. The ionic cores were described with projector augmented wave pseudopotentials<sup>55</sup>, and the wavefunction kinetic energy cutoff was set to 80 Ry to ensure high accuracy for molecular species. The energies were converged to  $10^{-4}$  eV and the forces were converged to less than  $0.02$  eV  $\text{\AA}^{-1}$ . The electronic states were treated with Gaussian smearing of  $0.007$  Ry width. Further calculations were conducted with Methfessel–Paxton smearing<sup>56</sup> to confirm that the results did not change substantially. All calculations were performed in the gas phase under the assumptions that the solvation free energies are the same for the isotopologues and therefore cancel in the calculation of  $\Delta E_{\text{ads}}$ , and that the effects of solvation on the geometries and normal modes are negligible.

The Pt(111) surface was modeled as a  $4 \times 4 \times 4$  slab, where the top two layers were allowed to relax from their optimized bulk positions following adsorption of OH or OD. A  $5 \times 5 \times 1$  *k*-point mesh was used, and periodic images were separated by  $37$   $\text{\AA}$  of vacuum in the surface normal direction. The adsorbed OH or OD was modelled at low (1/16 ML) and high (1/3 ML) coverages adsorbed on a top site, consistent with the minimum energy site observed in previous calculations<sup>57–60</sup>. The vibrational normal modes for the \*OL systems were calculated with the PHonon module of Quantum ESPRESSO<sup>30,51</sup> including only the atoms of the adsorbate. The ZPE and vibrational entropy contributions at 298 K were calculated for the adsorbed species from the modes corresponding to quasi-molecular vibrations (Supplementary Tables 6 and 7). For \*OL, these modes corresponded to the O–L stretching mode, the O–L bending mode and the Pt–O stretching mode. The vibrational modes of the platinum slab were assumed to be the same for the isotopologues and were not calculated. The translational and rotational entropy contributions for the adsorbed species were assumed to be negligible.

For the molecular species, the geometries were optimized in vacuum with a  $15 \text{ \AA} \times 15 \text{ \AA} \times 15 \text{ \AA}$  cubic unit cell and a  $1 \times 1 \times 1$  *k*-point mesh. The ZPE and vibrational entropy contributions at 298 K were calculated with the PHonon module for the molecular vibrational modes after removing the translational and rotational modes (Supplementary Table 8). The translational and rotational entropy contributions for the molecular species were obtained from DFT calculations with the PBE-D3 functional and the 6-31+G(d) basis set<sup>61–64</sup> at 298 K and 1 atm pressure using the Gaussian16 package<sup>65</sup> without periodicity (Supplementary Table 8). These rotational and translational entropic contributions were calculated both in the gas phase and in solvent; in both cases their effects on  $\Delta E_{\text{ads}}$  were negligible. However, a polarizable continuum solvent slightly impacts the ZPE and entropic contributions for  $\text{H}_2\text{O}$  and  $\text{D}_2\text{O}$  due to small changes in the vibrational frequencies. A comparison between the ZPE and entropic contributions in the gas phase, and using the polarizable continuum model<sup>66</sup> treatment of aqueous solvent computed with the Gaussian16 package for the PBE-D3 functional, is given in Supplementary Table 9. The gas-phase ZPE values listed in Supplementary Tables 7 and 9 differ slightly due to the use of a plane wave basis set in Quantum ESPRESSO for the values in Supplementary Table 7, and a Gaussian basis set in Gaussian16 for Supplementary Table 9. Using the ZPE and vibrational entropy contributions from the gas-phase Gaussian16 calculations for  $\text{H}_2\text{O}$  and  $\text{D}_2\text{O}$  shifts  $\Delta E_{\text{ads}}$  by only  $-0.1$  mV, and using the ZPE and vibrational entropy contributions from the polarizable continuum model solvent Gaussian16 calculations for  $\text{H}_2\text{O}$  and  $\text{D}_2\text{O}$  shifts  $\Delta E_{\text{ads}}$  by only  $-0.6$  mV. These entropies were obtained at 1 atm; using the vapour pressures of  $\text{H}_2\text{O}$  and  $\text{D}_2\text{O}$  at 300 K—as used previously for  $\text{H}_2\text{O}$  (ref. 33)—would shift the  $\Delta E_{\text{ads}}$  by  $\sim 3$  mV, but this strategy could potentially be considered inconsistent with gas-phase calculations. Moreover, the effects of hydrogen bonding on the vibrational frequencies are expected to be similar for  $\text{H}_2\text{O}$  and  $\text{D}_2\text{O}$ , and therefore are assumed to approximately cancel in the calculation of  $\Delta E_{\text{ads}}$ . The ZPE and vibrational entropy for \*OH and \*OD could only be calculated in vacuum using Quantum ESPRESSO. For consistency between the adsorbed and molecular species, the periodic DFT values

for the ZPE and vibrational entropy contributions computed with Quantum ESPRESSO were used for H<sub>2</sub>O and D<sub>2</sub>O in the reported values of  $\Delta E_{\text{ads}}$  (Supplementary Table 7).

The Pt(111) lattice constant was calculated to be 3.98 Å and 3.97 Å using the revPBE-D3 and PBE-D3 functionals, respectively. These values are in good agreement with the experimental value of 3.92 Å (ref. 67). The calculated frequencies and total entropies of the gas-phase molecular species are in good agreement with experimental values (Supplementary Tables 6 and 7)<sup>68</sup>. The major contributions to the ZPE for the surface adsorbates arise from the O–L stretching mode. Supplementary Table 10 provides the contributions of adsorbed species and molecular species to the calculated  $\Delta E_{\text{ads}}$ .

The relative equilibrium potentials for adsorbing OH or OD are determined according to equation (9) and are given in Supplementary Table 11. Using the revPBE-D3 functional, we predict that the \*OD peak would be shifted by –9.6 mV relative to the \*OH peak at both 1/16 ML and 1/3 ML coverages. This shift is consistent with the –11 mV shift observed in experiments for 0.1 M NaOH conditions. Using the offset  $eE_{\text{RDE}} - eE_{\text{RHE}}$  mentioned earlier, we predict that the \*OD peak would be 41.4 mV positive relative to the \*OH peak in acidic conditions. This prediction is in reasonable agreement with the experimentally measured shift of  $\Delta E_{\text{ads}} = 32$  mV in acidic conditions. Performing the same calculations with the PBE-D3 functional results in changes of  $\Delta E_{\text{ads}}$  on the order of 0.8 mV. The results are thus independent of surface coverage and functional for the cases studied.

## Data availability

Source Data are provided with this paper.

## References

- ASTM D1193-99e1: Standard Specification for Reagent Water (ASTM International, 1999).
- Milli-Q Direct Water Purification System: Pure and Ultrapure Water Directly From Tap Water PB1032ENUS (EMD, 2020).
- Amarego, W. L. F. & Perrin, D. D. in *Purification of Laboratory Chemicals* 4th edn (Elsevier, 1996).
- Monteiro, M. C. O. & Koper, M. T. M. Alumina contamination through polishing and its effect on hydrogen evolution on gold electrodes. *Electrochem. Acta* **325**, 134915 (2019).
- Agarwal, R. Determination and application of hydrogen transfer thermochemistry: studies of molecules, nanoparticles, and metallic electrodes. PhD thesis, Univ. Yale (2021).
- Clavilier, J., Faure, R., Guinet, G. & Durand, R. Preparation of monocrystalline Pt microelectrodes and electrochemical study of the plane surfaces cut in the direction of the {111} and {110} planes. *J. Electroanal. Chem.* **107**, 205–209 (1980).
- Attard, G. A. et al. The voltammetry of surfaces vicinal to Pt{110}: structural complexity simplified by CO cooling. *J. Electroanal. Chem.* **793**, 137–146 (2017).
- Rossmesl, J., Skúlason, E., Björketun, M. E., Tripkovic, V. & Nørskov, J. K. Modeling the electrified solid–liquid interface. *Chem. Phys. Lett.* **466**, 68–71 (2008).
- Jerkiewicz, G. Standard and reversible hydrogen electrodes: theory, design, operation, and applications. *ACS Catal.* **10**, 8409–8417 (2020).
- McIntyre, J. D. E. & Salomon, M. Kinetic isotope effects in the hydrogen electrode reaction. *J. Phys. Chem.* **72**, 2431–2434 (1968).
- Lam, Y.-C., Soudackov, A. V. & Hammes-Schiffer, S. Theory of electrochemical proton-coupled electron transfer in diabatic vibronic representation: application to proton discharge on metal electrodes in alkaline solution. *J. Phys. Chem. C* **124**, 27309–27322 (2020).
- Giannozzi, P. et al. QUANTUM ESPRESSO: a modular and open-source software project for quantum simulations of materials. *J. Condens. Matter Phys.* **21**, 395502 (2009).
- Giannozzi, P. et al. Advanced capabilities for materials modelling with Quantum ESPRESSO. *J. Condens. Matter Phys.* **29**, 465901 (2017).
- Zhang, Y. & Yang, W. Comment on “Generalized gradient approximation made simple”. *Phys. Rev. Lett.* **80**, 890–890 (1998).
- Grimme, S. Semiempirical GGA-type density functional constructed with a long-range dispersion correction. *J. Comput. Chem.* **27**, 1787–1799 (2006).
- Perdew, J. P., Burke, K. & Ernzerhof, M. Generalized gradient approximation made simple. *Phys. Rev. Lett.* **77**, 3865–3868 (1996).
- Dal Corso, A. Pseudopotentials periodic table: From H to Pu. *Comput. Mater. Sci.* **95**, 337–350 (2014).
- Methfessel, M. & Paxton, A. T. High-precision sampling for Brillouin-zone integration in metals. *Phys. Rev. B* **40**, 3616–3621 (1989).
- Liu, S., White, M. G. & Liu, P. Mechanism of oxygen reduction reaction on Pt(111) in alkaline solution: importance of chemisorbed water on surface. *J. Phys. Chem. C* **120**, 15288–15298 (2016).
- Anderson, A. B., Uddin, J. & Jinnouchi, R. Solvation and zero-point-energy effects on OH(ads) reduction on Pt(111) electrodes. *J. Phys. Chem. C* **114**, 14946–14952 (2010).
- Sakong, S., Naderian, M., Mathew, K., Hennig, R. G. & Groß, A. Density functional theory study of the electrochemical interface between a Pt electrode and an aqueous electrolyte using an implicit solvent method. *J. Chem. Phys.* **142**, 234107 (2015).
- Kristoffersen, H. H., Vegge, T. & Hansen, H. A. OH formation and H<sub>2</sub> adsorption at the liquid water–Pt(111) interface. *Chem. Sci.* **9**, 6912–6921 (2018).
- Ditchfield, R., Hehre, W. J. & Pople, J. A. Self-consistent molecular-orbital methods. IX. An extended Gaussian-type basis for molecular-orbital studies of organic molecules. *J. Chem. Phys.* **54**, 724–728 (1971).
- Hehre, W. J., Ditchfield, R. & Pople, J. A. Self-consistent molecular orbital methods. XII. Further extensions of Gaussian-type basis sets for use in molecular orbital studies of organic molecules. *J. Chem. Phys.* **56**, 2257–2261 (1972).
- Hariharan, P. C. & Pople, J. A. The influence of polarization functions on molecular orbital hydrogenation energies. *Theor. Chim. Acta* **28**, 213–222 (1973).
- Francl, M. M. et al. Self-consistent molecular orbital methods. XXIII. A polarization-type basis set for second-row elements. *J. Chem. Phys.* **77**, 3654–3665 (1982).
- Frisch, M. J. et al. *Gaussian 16 Rev. C.01* (Wallingford, 2016).
- Scalmani, G. & Frisch, M. J. Continuous surface charge polarizable continuum models of solvation. I. General formalism. *J. Chem. Phys.* **132**, 114110 (2010).
- Sakong, S., Naderian, M., Mathew, K., Hennig, R. G. & Groß, A. Density functional theory study of the electrochemical interface between a Pt electrode and an aqueous electrolyte using an implicit solvent method. *J. Chem. Phys.* **142**, 234107 (2015).
- NIST Chemistry WebBook: NIST Standard Reference Database Number 69* (eds. Lindstrom, P. J. & Mallard, W. G.) (National Institute of Standards and Technology, 2022).

## Acknowledgements

This work was primarily supported by the Center for Alkaline-Based Energy Solutions (CABES), part of the Energy Frontier Research Center (EFRC) program supported by the US Department of Energy, under grant no. DE-SC-0019445. R.G.A. and J.M.M. acknowledge funding from the Molecular Electrochemistry Multi-University Research Initiative (MURI) supported by the US Air Force Office of Scientific Research, under grant nos. FA9550-18-1-0420; the US National Science Foundation award no. CHE-1904813 for support; and a supplement that supported R.G.A.'s visit to the Koper laboratory in

Leiden. P.H. and R.G. acknowledge support from National Science Foundation Graduate Research Fellowships. R.R., E.H. and J.M.F. acknowledge funding from Ministerio de Ciencia e Innovación (Spain) under grant no. PID2019-105653GB-I00. R.G.A. would also like to thank M. Koper and the members of his laboratory for their hospitality during his short stay in Leiden, and for introducing him to the challenges of preparing high-purity D<sub>2</sub>O.

### Author contributions

Y.Y. and H.D.A. conceived the project. Y.Y. performed electrochemical measurements with help from X.L. R.R. independently verified the experimental results under the guidance of E.H. and J.M.F. R.G.A. developed the D<sub>2</sub>O purification method under the guidance of J.M.M. P.H. and A.V.S. performed DFT simulations under the guidance of S.H.-S. All of the authors discussed the results and approved the manuscript.

### Competing interests

The authors declare no competing interests.

### Additional information

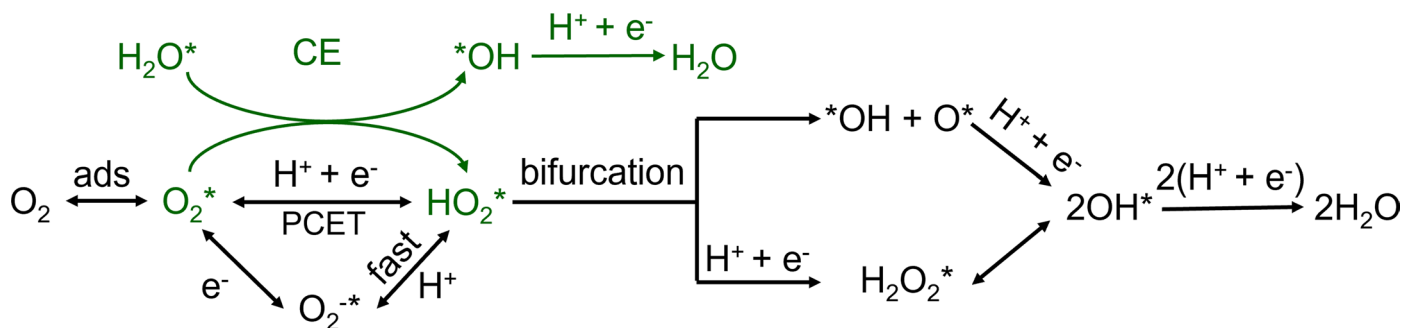
**Extended data** is available for this paper at <https://doi.org/10.1038/s41557-022-01084-y>.

**Supplementary information** The online version contains supplementary material available at <https://doi.org/10.1038/s41557-022-01084-y>.

**Correspondence and requests for materials** should be addressed to Enrique Herrero, Juan M. Feliu, Sharon Hammes-Schiffer, James M. Mayer or Héctor D. Abruña.

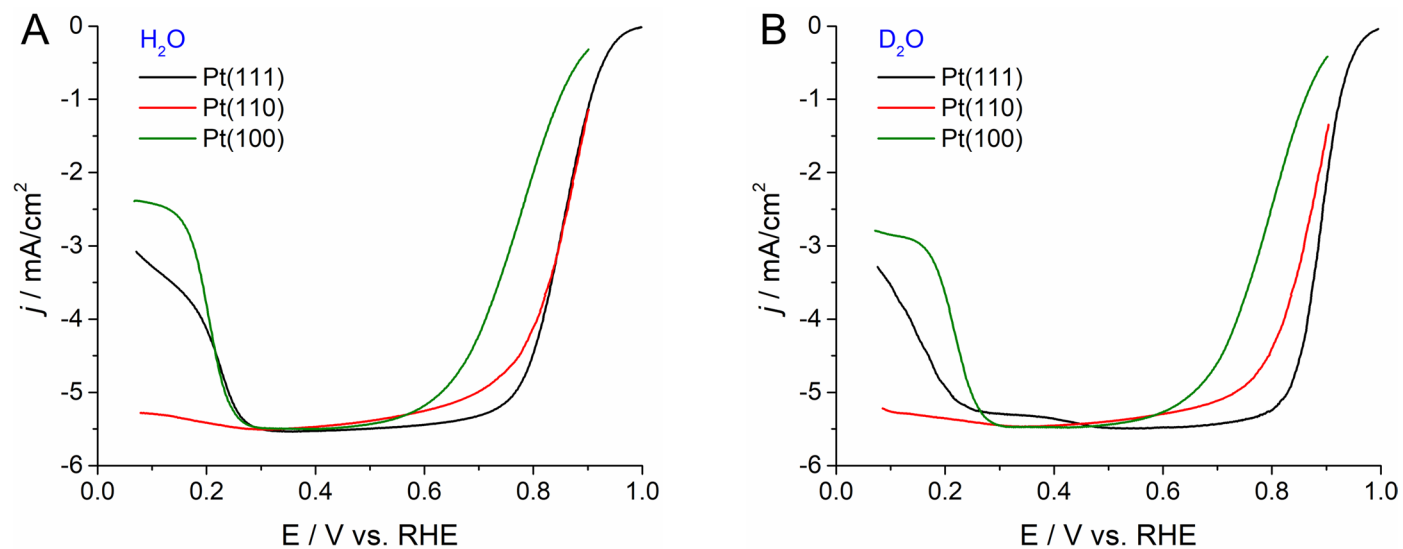
**Peer review information** *Nature Chemistry* thanks Henrik Kristoffersen, Vojislav Stamenkovic and the other, anonymous, reviewer(s) for their contribution to the peer review of this work.

**Reprints and permissions information** is available at [www.nature.com/reprints](http://www.nature.com/reprints).

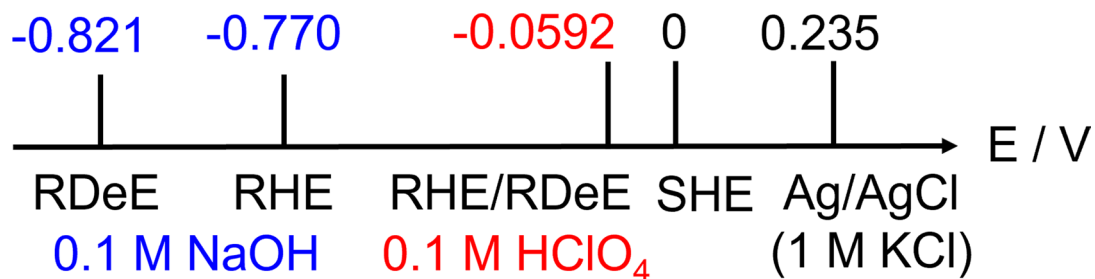


**Extended Data Fig. 1 | A simplified mechanism proposed for the oxygen reduction reaction (ORR) in acid.** Reaction pathways have been established based on extensive studies on Pt surfaces and may be applicable to other types of catalysts. A superscript \* by an intermediate indicates a reaction intermediate adsorbed on the electrocatalytic surface. The CE mechanism in acid, marked

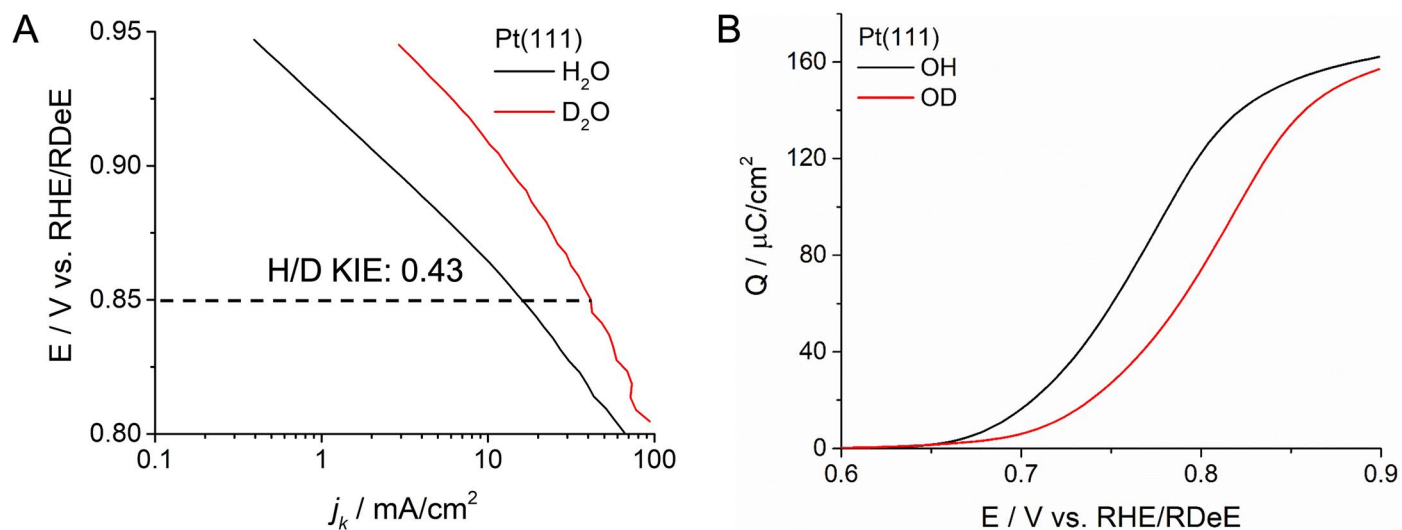
in green, represents a fast surface chemical reaction preceding an irreversible one-electron transfer process. PCET stands for proton-coupled electron transfer process.  $H_2O$  serves as the proton donor in alkaline media. Solution species were not included for simplicity. Complete ORR mechanisms in acid and base can be found in Supplementary Fig. 5.



**Extended Data Fig. 2 | Comparisons of ORR polarization profiles of three low-index Pt single crystals in acidic H<sub>2</sub>O and D<sub>2</sub>O.** Comparisons of ORR polarization profiles of three low-index Pt single crystals in O<sub>2</sub>-saturated 0.1 M HClO<sub>4</sub> in H<sub>2</sub>O (A) and D<sub>2</sub>O (B).



**Extended Data Fig. 3 | Potential axis.** Potential axis showing that the RDeE is equal to the RHE in acid (for example 0.1 M HClO<sub>4</sub>, pH = 1) but is more negative than the RHE by 51 mV in base (for example 0.1 M NaOH, pH = 13) due to the difference in pK<sub>a</sub> in H<sub>2</sub>O (14) and D<sub>2</sub>O (14.87).



**Extended Data Fig. 4 | Tafel plots of Pt(111) and  $^*OD/^*OH$  adsorption coverage in base.** (A) Tafel plots of Pt(111) in  $O_2$ -sat. 0.1 M NaOH in  $H_2O$  and  $D_2O$  at 1600 rpm based ORR polarization profiles in Supplementary Fig. 6. (B)  $^*OD$  and  $^*OH$  adsorption coverage on Pt(111) in alkaline  $D_2O$  and  $H_2O$  as a function of potentials extracted from Fig. 4A.